Atomistic simulations of geopolymer models: the impact of disorder on structure and mechanics.

Francesca Lolli,[†] Hegoi Manzano,[‡] John L. Provis,[¶] Maria Chiara Bignozzi,[§] and Enrico Masoero*,[†]

†*School of Engineering, Newcastle University, Newcastle Upon Tyne, United Kingdom*

‡*Condensed Matter Physics Department, University of the Basque Country (UPV/EHU), Bilbao, Spain*

¶*Department of Materials Science and Engineering, University of Sheffield, Sheffield, United Kingdom*

§*Dipartimento di Ingegneria Civile, Chimica, Ambientale e dei Materiali, University of Bologna, Bologna, Italy*

E-mail: enrico.masoero@newcastle.ac.uk

Abstract

Geopolymers are hydrated alumino-silicates with excellent binding properties. Geopolymers appeal to the construction sector as a more sustainable alternative to traditional cements, but their exploitation is limited by a poor understanding of the linkage between chemical composition and macroscopic properties. Molecular simulations can help clarify this linkage, but existing models based on amorphous or crystalline aluminosilicate structures provide only a partial explanation of experimental data at the nanoscale. This paper presents a new model for the molecular structure of geopolymers,

in particular for nanoscale interfacial zones between crystalline and amorphous nano-domains, which are crucial for the overall mechanical properties of the material. For a range of Si:Al molar ratios and water contents, the proposed structures are analysed in terms of skeletal density, ring structure, pore structure, bond-angle distribution, bond length distribution, X-ray diffraction, X-ray pair distribution function, elastic moduli, and large-strain mechanics. Results are compared with experimental data and with other simulation results for amorphous and crystalline molecular models, showing that the newly proposed structures better capture important structural features with impact on mechanical properties. This offers a new starting point for the multi-scale modelling of geopolymers.

Keywords

Geopolymers, Atomistic simulation, Molecular structure, Mechanical properties, XRD, X Ray PDF, Sodalite.

1 Introduction

Geopolymers, or more appropriately low-calcium alkali-activated aluminosilicate cement, are inorganic solids obtained from alumino-silicate precursors such as calcined clays *e.g.* metakaolin $2SiO_2{\cdot}Al_2O_3$, or industrial by-products, *e.g* pulverised fuel ash (PFA) or ground granulated blast furnace slag (GGBS). These precursors are activated with alkaline aqueous solutions, usually based on sodium and potassium, which induce the dissolution of the precursors and the polymerisation of AlO_2 and SiO_2 tetrahedra into a three-dimensional network at the molecular scale. Some water remains physisorbed while the cations (Na^+ or K^+) are bound ionically, providing positive charges that maintain overall neutrality and allow for the Al to be tetra-coordinated. The macroscopic outcome of this reaction is analogous to the hydration of a cement paste, *viz.* the setting of a hard binding phase. This so-called "geopoly-

merisation" reaction,[1] however, is fundamentally different from the hydration of traditional portland cements and indeed the production of geopolymer binders causes significantly less CO_2 emissions compared to portland cement.[2] It is for this reason that geopolymers appeal to the construction industry, along with their good mechanical strength, as well as thermal and acid resistance.[3] On the other hand, the exploitation of geopolymer cements is still limited by the inability to predict and control their durability. This calls for a better understanding of the linkage between chemical composition and degradation mechanisms.[4] Molecular simulations and nanoscale modelling provide a possible pathway to address this challenge.

In the field of traditional cement science, molecular models of key hydration products[5–7] have provided a starting point for a multiscale modelling approach that is now starting to clarify the nanoscale origin of degradation mechanisms such as creep and shrinkage.[8–10] The multiscale modelling of geopolymers is less developed, with the first molecular simulations having been carried out only very recently.[11,12] Molecular models used in some geopolymer simulations today are based on fully amorphous (glassy) structures. Experimental characterisation of these material does indeed show features that are typical of amorphous molecular structures: a broad peak in X-ray diffraction (XRD) between 2θ= 25°- 35°, amorphous regions in transmission electron microscopy (TEM) images, an X-ray pair distribution function (PDF) with only low intensity peaks beyond 5 Å atomic correlation distance.[13] On the other hand, the same experiments also show features that are typical of crystalline (or partially crystalline) structures: XRD peaks corresponding to faujasite, sodalite and zeolite A (especially in samples prepared at high temperature, *e.g.* 85°C[14]), corresponding short-range peaks in the X-ray pair distribution function,[13] and crystalline domains in TEM images.[15] To reconcile these data, geopolymers are sometimes described as nanocrystalline zeolitic networks within an amorphous alumino-silicate binding gel: the so-called "pseudo-crystalline" model.[16] This leads to two possible scenarios:

1. if one considers the geopolymer as a uniform phase at the molecular scale, than this

phase must be intermediate between amorphous and crystalline;

2. if one refers to the pseudo-nanocrystalline model, then the interfacial zones between nanocrystals and amorphous gel must be intermediate between the two, and are likely to significantly impact the overall composite mechanics.

Both of these scenarios call for a representation of geopolymer molecular structures intermediate between glassy and crystalline, which is the contribution of this paper.

This paper presents a new molecular model to describe the geopolymerisation product of sodium silicate activated metakaolin, hereafter referred to as N-A-S-H (sodium-aluminium-silicate-hydrate). The model is based on a defective crystal structure, obtained by creating vacancies into a sodalite cage and rearranging atoms to respect Loewenstein's principle [1] and full Q^4 polymerisation of Al and Si tetrahedra, as indicated by experimental data [17,18]. Skeletal density, ring structure, pore structure, bond-angle distribution, bond length distributions, X-ray diffraction, X-ray pair distribution function and mechanical properties (tensile stress-strain curves and non-affine displacements) are computed for a range of Si:Al molar ratios and water contents, and then compared with available experimental data. Fully amorphous and fully crystalline model structures are also analysed, to assess the impact of disorder at the molecular scale.

2 Methodology

2.1 Siliceous baseline structures

Geopolymer molecular structures are created with different chemical compositions, described by Si:Al molar ratios of 1, 2 and 1.4-1.5 as shown in Table 1.

To consider different levels of disorder, three types of structure are built: a fully crystalline, a fully amorphous, and a defective crystal structure. The starting point is to construct a baseline structure containing only Si and O atoms: not including Al and Na in the initial

Table 1: The three molecular structures studied here: amorphous (Am), crystalline (Cr) and with defects (De). The Na:Al:H_2O molar ratio are set to 1:1:3 for all structures. *Total number of H and O atoms in water molecules divided by the total number of atoms in the cell.

Name	Si:Al molar ratio	Chemical formula	Cell volume (nm^3)	Atoms in simulation cell	Water content (atom % *)
Am_1.5	1.5	$3\,SiO_2 \cdot 2\,Al_2O_3 \cdot 2\,Na_2O \cdot 6\,H_2O$	41.26	4324	51.4
Am_2	2	$4\,SiO_2 \cdot 2\,Al_2O_3 \cdot 2\,Na_2O \cdot 6\,H_2O$	38.73	3914	47.4
Cr_1	1	$2\,SiO_2 \cdot 2\,Al_2O_3 \cdot 2\,Na_2O \cdot 6\,H_2O$	54.25	6144	56.3
Cr_1.4	1.4	$2.8\,SiO_2 \cdot 2\,Al_2O_3 \cdot 2\,Na_2O \cdot 6\,H_2O$	50.07	5496	52.4
Cr_2	2	$4\,SiO_2 \cdot 2\,Al_2O_3 \cdot 2\,Na_2O \cdot 6\,H_2O$	52.53	4856	47.4
De_1.5	1.5	$3\,SiO_2 \cdot 2\,Al_2O_3 \cdot 2\,Na_2O \cdot 6\,H_2O$	44.95	4480	51.4
De_2	2	$4\,SiO_2 \cdot 2\,Al_2O_3 \cdot 2\,Na_2O \cdot 6\,H_2O$	46.03	3840	45.0

baseline structures enables a clearer characterisation of their skeletal structures. Adding Al and Na causes structural distortions, mainly because the Na cations tend to find their equilibrium positions at the centre of the sodalite rings, altering the (Si,Al)-O-Si bond angles *via* electrostatic interactions. The Si-O baseline structures are first energy-minimised at T= 0 K and P= 1 atm, using the Polak-Ribiere version of the conjugate gradient method implemented in LAMMPS.[19] The baseline structures are then characterised using ISAACS,[20] quantifying in particular the bond length, bond angle, ring distributions, and pore size distribution. The ring distribution is computed using the King's shortest path criterion, with a ring being a closed path of nodes (Si atoms) and links (Si-O-Si bonds) connected in sequence without overlap.[20] The pore size distributions are obtained using the method by Pinhero et al.,[21] with probe radius of 0.1 Å (after checking convergence starting from probe radius of 1 Å and progressively reducing it). This method is based on Voronoi tassellation and is implemented in the open source package Zeo++.[22]

2.2 Introduction of Al, Na and water

To convert the Si-O only structures into model N-A-S-H structures (crystalline, amorphous and defective), Si atoms are substituted by Al and Na atoms, and water molecules are added with initially random positions using the software Packmol[23] as shown in Fig. 1. Periodic

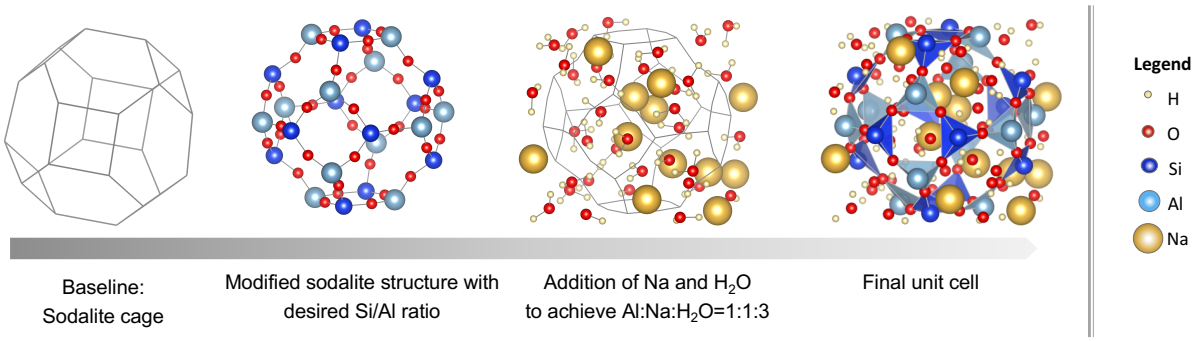

Figure 1: Simplified schematic of the construction process for a crystalline structure. All snapshots are obtained using VESTA.[24]

boundary conditions are applied in all three directions, and the principles followed for all structures are:

1. The number of added Na atoms is equal to the number of Al atoms in the structure, to satisfy charge neutrality, since Al is tetracoordinated and thus the Al-centred tetrahedron carries a net negative charge in the structure.

2. Three molecules of water (hereafter referred to as "structural water") are added for each Na atom. Structural water is defined as the minimum amount of water below which the material will undergo microstructural changes leading to drying shrinkage and microcracks. Drying shrinkage experiments have shown that extensive shrinkage deformations start only when the H_2O:Na molar ratio decreases below 3. Such a threshold ratio of *ca.* 3 has emerged from experiments in which geopolymer samples with Si:Al = 1.15 - 2.15 and H_2O:Na molar ratio = 5.5 were dried at 150°C.[25] The drying caused a weight loss between 20% and 40% of the initial sample weight that, given the stoichiometry of the tested samples, was found to be consistent with a molar ratio H_2O:Na = 3.3 - 4.4 for water that is still present in the geopolymer at 150°C. Similarly, Kuenzel et al.[26] ran a series of drying shrinkage experiments on geopolymer samples showing that, irrespective of the initial amount of water in the mix, extensive

shrinkage started only when the residual water content decreased below H_2O:Na = 3. Thus, H_2O:Na=3:1 is considered to be a reasonable estimation of structural water content in the N-A-S-H skeleton.

3. Loewenstein's principle is always respected, meaning that two Al tetrahedra cannot be linked by a single oxygen bond, and therefore each Al tetrahedron is always linked to four Si tetrahedra.[1] In reality, Na-based geopolymers display some Al-O-Al bonds but to such a small extent (*e.g.* 0.18% of T-O-T total bonds for Si/Al = 1.15[27]) that imposing a complete absence of Al-O-Al bonds leads to model structures that are more statistically relevant than what would be obtained if this constraint were removed.

4. No edge-sharing Al tetrahedra. When creating amorphous or defective structures with Al and Si tetrahedra, *e.g.* via heating-quenching or packing simulations, some tetrahedra often get linked to each other twice *via* two oxygen bonds.[11] This leads to a significant stretching of some O-T-O angles, which is thermodynamically unfavourable and unphysical when considering a room-temperature, hydrous structure. This may have a significant effect on the prediction of mechanical properties.

5. Full Q^4 polymerisation, to obtain structures that are most statistically relevant, in agreement with the results of Al and Si nuclear magnetic resonance (NMR) experiments[17].[18]

2.3 Structural and mechanical characterisation

The N-A-S-H structures are first relaxed *via* energy minimisation, using the Polak-Ribiere version of the conjugate gradient method in LAMMPS.[19] The structures are then equilibrated at P = 1 atm and T = 300 K *via* 1 ns of molecular dynamics in the NPT ensemble, also performed using LAMMPS (Verlet time integration scheme and integration timestep of 0.1 fs). The NPT simulations are followed by 1 ns in the NVT ensemble, to verify the stability of potential energy and pressure. All the simulations employed the ReaxFF inter-

action potential.[28] In ReaxFF the interatomic bonding expressions are both bond-distance and bond-order dependent, and the atomic charges to compute the long range coulombic interaction are calculated on the fly by a charge equilibration method. As a result, ReaxFF is a very flexible force field, and can reproduce chemical reactions for a wide range of structures. For instance, the same set of parameters can be used for the study of glasses and crystals with good accuracy.[29,30] The force field parameters used in this work are based on the Si/O/H[31] set, extended with Al/O/H[32] parameters for the study of aluminosilicate frameworks, and improved with *a posteriori* specific parameterisation of the Si-O-Al angles and proton stability on aluminosilicate rings.[33] These parameters have been previously used to investigate silicalite and H-ZSM-5 aluminosilicate zeolites, their thermal stability, and their acid site chemistry.[32–34] In addition, the Si/O/H subset has been shown to reproduce the structural features of amorphous (sodium) silicate glasses.[35,36] To verify the ability of the chosen parameters to produce realistic elastic properties of aluminosilicates, the elastic tensor of faujasite has been computed, a sodalite-based zeolite with structural resemblance to geopolymers. The NaX faujasite analogue structure[37] was minimised using ReaxFF and its elastic properties were obtained from the elastic tensor coefficients.[38] The unit cell parameters are in good agreement with the experimental ones, with limited difference in volume (1.4%, as shown in Table 2). The cubic symmetry is broken due to finite size effect of the simulation box and the consequent irregular distribution of Na counterions. The bulk modulus (K) of the zeolite is in very good agreement with the experimental measurement[39] and DFT simulations[40] as shown in Table 2.

Table 2: Comparison between literature data on faujasite and parameters obtained in this study as part of the validation of the ReaxFF potential.

Faujasite	Lattice parameters (Å)	K (GPa)
Obtained values	a=24.93	
	b=25.16	36
	c=25.56	
Literature data	a=b=c=25.10	38.7,[39]35[40]

The equilibrated N-A-S-H structures are then analysed in terms of structural features and mechanical properties. The X-Ray diffraction patterns were simulated using the CrystalDiffract 6.5.0 program[41] . The patterns were generated using an instrumental peak broadening of 0.5^o full width at half-maximum. ISAACS is used to compute the Fourier transform of the structure factor obtained using the Debye equation,[20] thus producing the X-Ray pair distributions. Mechanical tests are simulated with LAMMPS[19] through tensile deformation of each simulation box by 1% of its length per step until rupture: strain increments in this range are typical in molecular simulations, where the absence of macroscopic defects enables significantly higher strain and stress levels compared to similar tests performed at the macroscale.[29] This increment has been chosen following a sensitivity analysis of different deformation steps (varying from 0.1% to 2.5% of the corresponding length of the box). After each deformation step the structures have been relaxed *via* energy minimisation (Polak-Ribiere version of the conjugate gradient method in LAMMPS[19]). The simulation box dimensions are kept fixed on the plane perpendicular to the loading direction: this generates a uniaxial strain scenario like in nanoindentation or in atomic force microscope indentation experiments.[42] The simulated tests lead to stress-strain curves akin to those in Fig. 2, from which one can compute elastic moduli, strength, and modulus of toughness. The strength is the maximum stress attained during the deformation process. The modulus of toughness is the area under the stress-strain curve; it quantifies the energy required to take a unit volume of material to complete failure. The elastic moduli quantify the amount of stress that produces a unit strain in the small-deformations regime, *viz.* when the strain tends to zero. The initial gradient of the stress-strain curve in Fig. 2 is the so-called indentation modulus M, which is an elastic modulus related to the Young's elastic modulus E and Poisson's ratio ν by:[43]

$$E = \frac{M(1+\nu)(1-2\nu)}{(1-\nu)} \tag{1}$$

Eq. 1 assumes that the material is homogeneous, isotropic, and linear elastic: all these conditions apply to the model structures in this paper, when the strain tends to zero. For

the uniaxial strain scenario considered in this paper, the Poisson's ratio, relates the stress in the loading direction i with the stress in its perpendicular directions j and k:[44]

$$\sigma_{jj} = \frac{\nu}{1-\nu}\sigma_{ii} \; ; \qquad \sigma_{kk} = \frac{\nu}{1-\nu}\sigma_{ii} \tag{2}$$

Eq. 2 allows computing the Poisson's ratio from the stresses in all three directions, these latter being tracked by LAMMPS at each step of the deformation process. The average magnitude of non-affine displacements $\overline{\delta}_{na}$ has also been computed as

$$\overline{\delta}_{na} = \frac{\sum_i^N |r_i(\varepsilon) - r_{i,aff}(\varepsilon)|}{N} \tag{3}$$

where N is the number of atoms in the simulation box, r_i is the position of atom i at the strain level ε after energy minimization at that strain level, and the affine $r_{i,aff}$ is the position that the same atom i would have had at the same strain level ε if no minimisation was ever performed during the tensile deformation test. Non-affine displacements typically correlate with the onset and accumulation of plastic deformations, hence with the ductility or brittleness of the structure.[45]

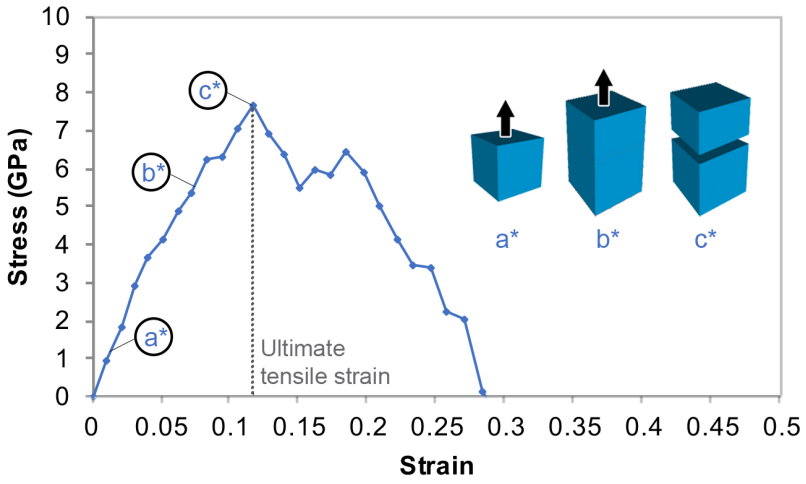

Figure 2: Stress-strain graphs for defective structure obtained through MD simulation.

2.4 Additional details depending on the level of disorder

Crystalline structures The crystalline structures built for this work are based on a simple sodalite framework which is common in zeolites[46] (see Fig. 1). Indeed, experiments on geopolymers obtained from metakaolin precursor show that, under certain conditions, faujasite and/or zeolite A can be formed,[47] whose basic building unit is the sodalite cage.[48–52]

Amorphous structures The starting structure for the amorphous N-A-S-H product is an amorphous SiO_2 glass developed by Sheikholeslam et al.[36] This has been preferred over the amorphous N-A-S-H model structures available in the literature[11] because the former satisfies all the constraints that we listed in Section "Introduction of Al, Na and water", in particular the Loewenstein's principle, the absence of edge-sharing tetrahedra, and the full Q^4 polymerisation of tetrahedra. A simple Monte Carlo program has been written and used to substitute Si with Al while respecting Loewenstein's principle. Only two Si:Al molar ratios (1.5 and 2) were created; Si:Al = 1 was not achievable due to the disordered topology.

Defective structures The design process for the defective structure is described in Fig. 3. The starting structure is the crystalline siliceous sodalite (without Al) equilibrated at P =1 atm. Two SiO_2 molecules are randomly deleted from the sodalite framework to create vacancies; this is followed by molecular dynamics simulations at P = 1 atm (NPT ensemble, 0.01 ns) and then in the NVT ensemble (0.01 ns). This leads to a defective structure with some O atoms left with dangling bonds. To restore full Q^4 polymerisation, individual atoms are slightly displaced by hand, then repeating the NPT equilibration until full polymerisation is recovered. At this stage of the structure preparation, the simulations are performed at T = 1000 K to accelerate and enable a more effective relaxation of the structure before inducing next alterations. Subsequently, the final structures are equilibrated to 300 K for 2 ns, as explained in Section 2.3, before proceeding to any further characterisation. This preparation protocol has the advantage of leading to structures with defects that nevertheless

present some traces of the original crystal. Other preparation approaches, such as quenching, would lead to structures that are significantly more disordered than the intermediate level of disorder targeted here. The desired Si:Al ratio is obtained with the same substitution procedure as for the amorphous structures.

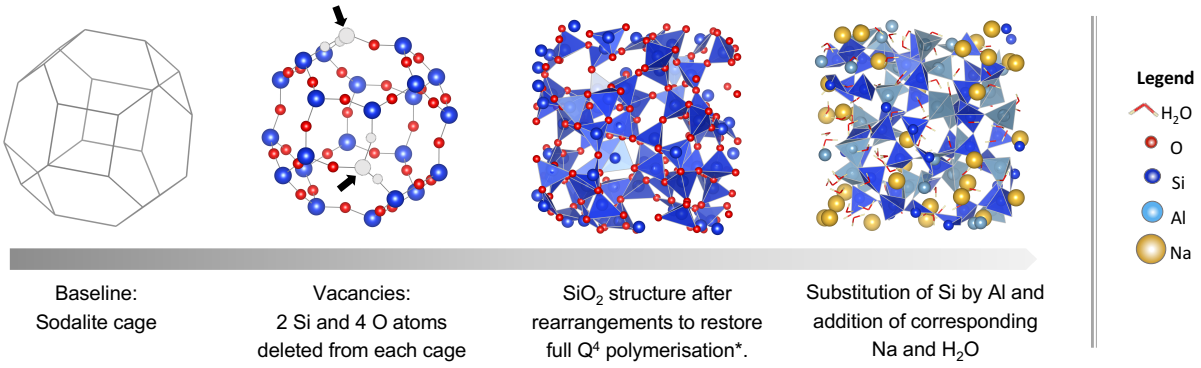

Figure 3: Simplified scheme of the construction process for a defective structure. All snapshots are obtained using VESTA.[24] *Some Si atoms are not visualised as tetrahedra due to the boundary conditions.

Overall, seven different model structures of N-A-S-H have been created and analysed: three crystalline, two amorphous and two defective. Fig. 4 shows equilibrated structures with similar Si:Al molar ratios and with the organisation of tetrahedra highlighted. An increasing degree of disorder is noticeable from left to right in Fig. 4.

3 Results

3.1 Siliceous baseline structures: bond angle, bond length, ring distributions, and pore structure.

Fig. 5 shows the distributions of internal (O-Si-O) and external bond angles (Si-O-Si). The internal angle quantifies the distortion of the tetrahedra, whereas the external angle measures the relative orientation of tetrahedra in the short range (first neighbour). Longer-range

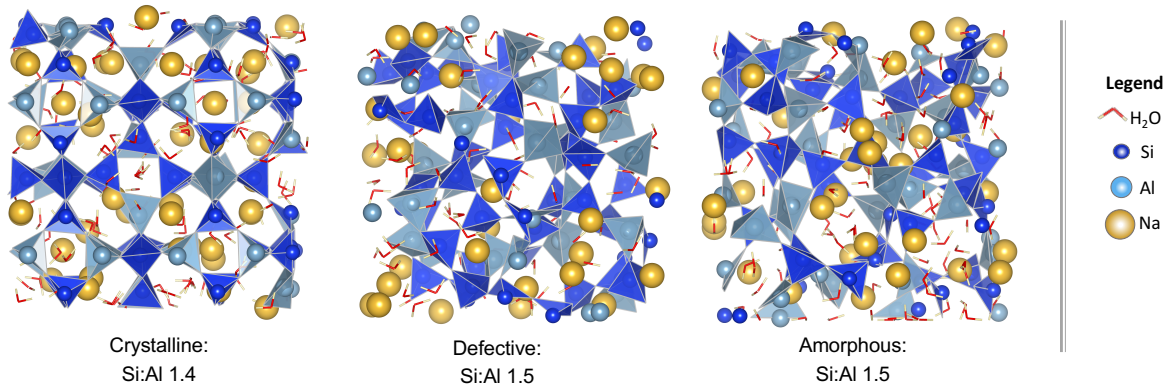

Figure 4: Structures with Si:Al = 1.4 - 1.5 and different degrees of disorder. The organisation of Al and Si tetrahedra is highlighted. All snapshots are obtained using VESTA.[24]

topological information will be discussed later in terms of ring analysis. For a tetrahedral Si-O coordination, the O-Si-O internal angle distribution is expected to display a sharp peak at 109°.[20] This is indeed the result for the crystalline model structure in Fig. 5. The amorphous and defective structures have a very similar distribution of O-Si-O angles, with a limited standard deviation, probably a consequence of the overall disorder. This indicates that the tetrahedra are only weakly distorted, and that there are no edge-sharing tetrahedra, as also confirmed by visual inspection of the configurations.

The distribution of external Si-O-Si angles shows that the crystalline structure has wider angles compared to the defective and amorphous structures, and that these latter two have similar distributions. Experiments shows that the T-O-T angles in polymerised SiO_2 and AlO_2 can range between 120° and 180°,[53,54] which agrees with Fig. 5. The smaller angles of the amorphous and defective structure compared to the crystalline structure, suggest that the formers may be folded to some extent, which should result into higher densities. This is confirmed by the density values of the siliceous structures calculated at zero pressure. The densities of the amorphous and defective structures are similar to each other and respectively equal to 2.28 g/cm^3 and 2.13 g/cm^3, whereas the crystalline structure has a lower density of 1.66 g/cm^3.

The Si-O bond length distribution in Fig. 6 corroborates this point: the mode of the

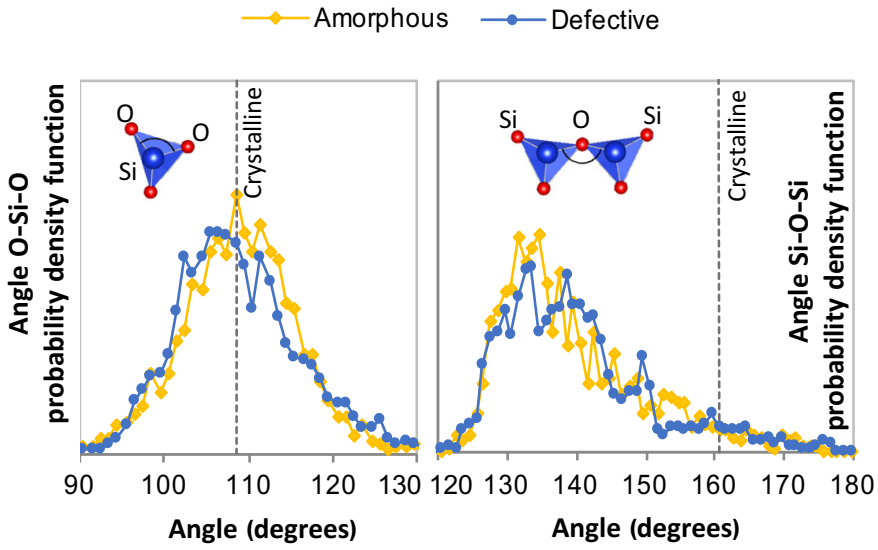

Figure 5: Internal (O-Si-O) and external (Si-O-Si) bond angle distributions for the three siliceous baseline structures. The area under the curve is normalised to the same constant.

distributions for the amorphous and defective structures are shifted to the left compared to the bond length value of the crystalline structure. These shorter bonds are consistent with the disordered siliceous structures being denser than the crystalline one.

The angle analysis in Fig. 5 highlights some differences between crystalline and disordered structures, but does not indicate any appreciable difference between defective and amorphous structures. Such a difference emerges instead the pore structure and topology of the structure over larger length scales. The ring analysis in Fig. 7 provides one such topological measure. The ring analysis of the crystalline structure is in good agreement with results in the zeolite literature, with prevalence of rings with size 4, 6, and 8 nodes.[55] The ring distributions of the amorphous and defective structures display a wider range of ring sizes, indicative of the greater medium-range disorder in these structures. Rings of odd size appear in both, and the range of possible sizes is significantly broader in the defective structure compared to the amorphous one, despite a similar size of the simulation cell and a similar number of atoms in the structure (see Table 1). The differences in ring size distribution between the amorphous and the defective structure may impact their mechanical performance. On one hand, larger

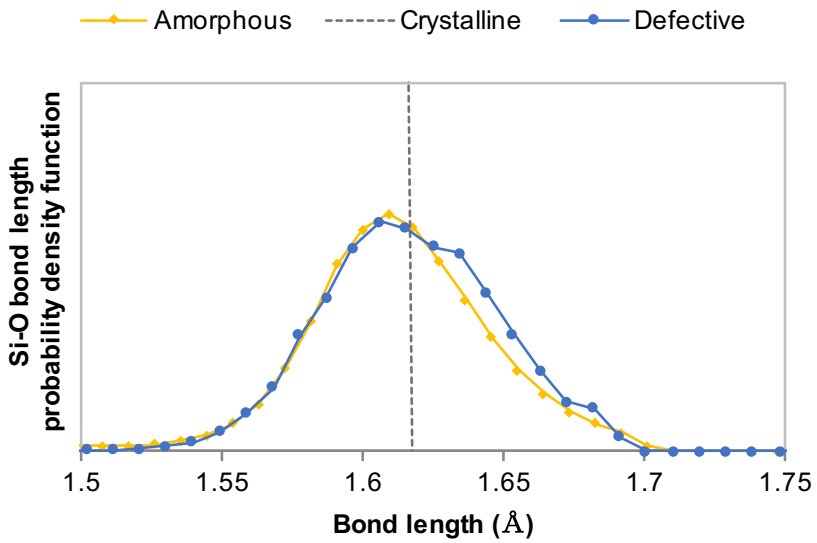

Figure 6: Bond length analysis of the three siliceous baseline structures (time averaged over 50 timesteps).

rings at the expense of smaller ones may indicate the presence of nanopores, which would decrease density and mechanical properties. On the other hand, the formation of large rings may provide long-range correlations that may improve the large-strain mechanics of the system. It is also useful to note that the amorphous and defective structure have very similar total energy per mole of Si, which means that they are equally probable in thermodynamic terms (as expected, the crystalline structure has instead a much lower energy).

Fig. 8 shows the pore size distribution of the crystalline structure, correctly peaked around a diameter of 6.5 Å, which is the characteristic size of the sodalite cage shown in the snapshot. As expected, the pore structure of the crystalline structure is fully interconnected. The amorphous structure, instead, has a fragmented pore structure with smaller diameters, peaked around 4 Å. The presence of small pores is related to the presence of small rings with size 3 in Fig. 7. The defective structure shows a pore structure that is indeed intermediate between those of the crystalline and of the amorphous structures. The pores are still interconnected to some extent, although less than in the crystalline structure (see snapshot in Fig. 8). Furthermore, the pore size distribution displays both a primary peak at *ca.* 4.5 Å,

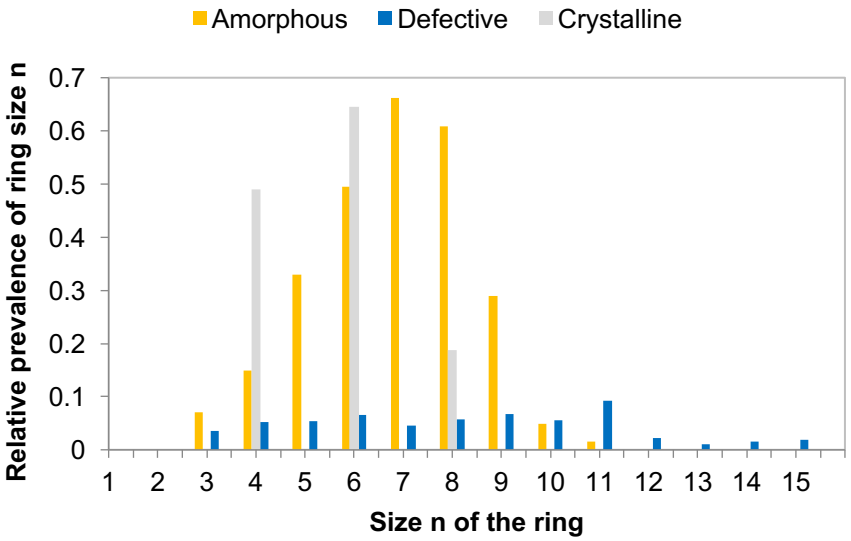

Figure 7: Ring size distribution of the siliceous baseline structures. The sum of all histograms is equal to the number of Si atoms.

close to that of the amorphous structure, and a secondary peak at 6.5 Å, which indicates some persisting features of the original crystal structure from which the defective one was obtained. The relationship between ring size distribution, pore structure, skeletal density and mechanical properties will be discussed.

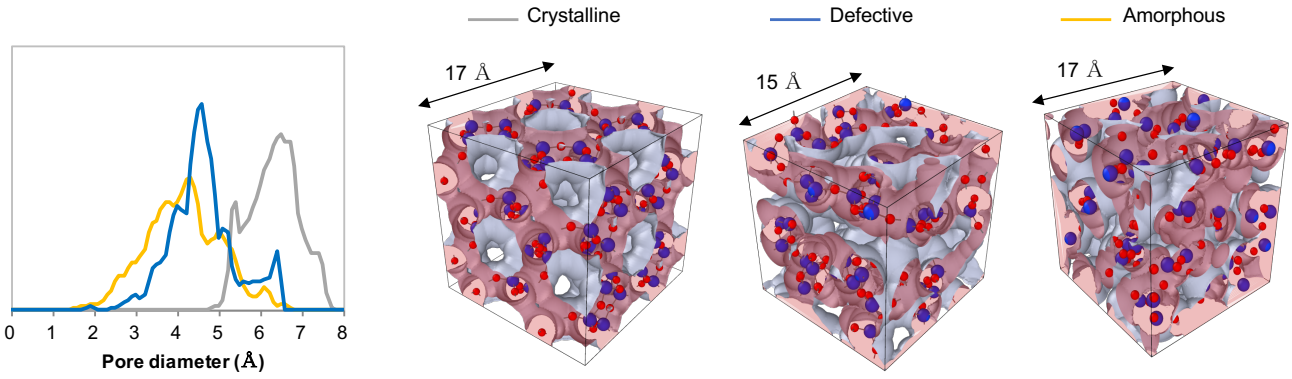

Figure 8: Pore size distribution and snapshots of the porosity of the siliceous structures. All snapshots are obtained using OVITO.[56]

3.2 X-ray diffraction (XRD)

Fig. 9 shows the comparison between experimental X-ray diffraction data and simulations, highlighting the effect of molecular disorder on the calculated XRD patterns of structures with comparable Si:Al ratios of 1.4-1.5. For all patterns a peak broadening has been applied as explained in the methodology. The experimental spectrum is from a metakaolin-based geopolymer paste with Si:Al = 1.5 cured at 23°C for 28 days. The simulations are not expected to precisely match the experimental spectrum, because the geopolymer is clearly not a pure crystal, thus structural disorder, defects, and impurities at all scales will introduce or smoothen features in the XRD signals which cannot be fully described by a molecular model only. However, two key features can be targeted and discussed in relation to the model molecular structures presented here: the broad peak that emerges at 2θ= 20°- 30°, which is typical of disordered alkali aluminosilicate gels, and the sodalite-related peaks at 2θ= 24° and 32°. From the simulated X-Ray diffraction pattern the increased degree of order from the amorphous to the crystalline structure is appreciable: the amorphous structure does not display meaningful peaks; the crystalline structure displays sharp peaks typical of sodalite; the defective structure shows an overall disordered character but with sharper peaks (sodalite and quartz peaks at 2θ=27°) compared to the amorphous structure. The red curve in Fig. 9 is the results of the summation of the three spectra of crystalline, amorphous and defective structure, considering that the sample has an equal amount of the three systems. The resulting pattern presents a broad peak between 2θ=25° and 2θ=40° which is clearly due to the contribution of the defective structure, while the amorphous system just adds a background noise. As a result, the defective structure better captures the coexistence of amorphous and crystalline features emerging from the experiments consistently with the two scenarios depicted in the introduction.

Fig. 10 shows that altering the Si:Al ratio has a very small impact on the overall XRD signal. By decreasing the Si:Al ratio (thus increasing the number of Al, Na, and H_2O) the sodalite peaks slightly shift towards larger values of the 2θ angle. This is true irrespective

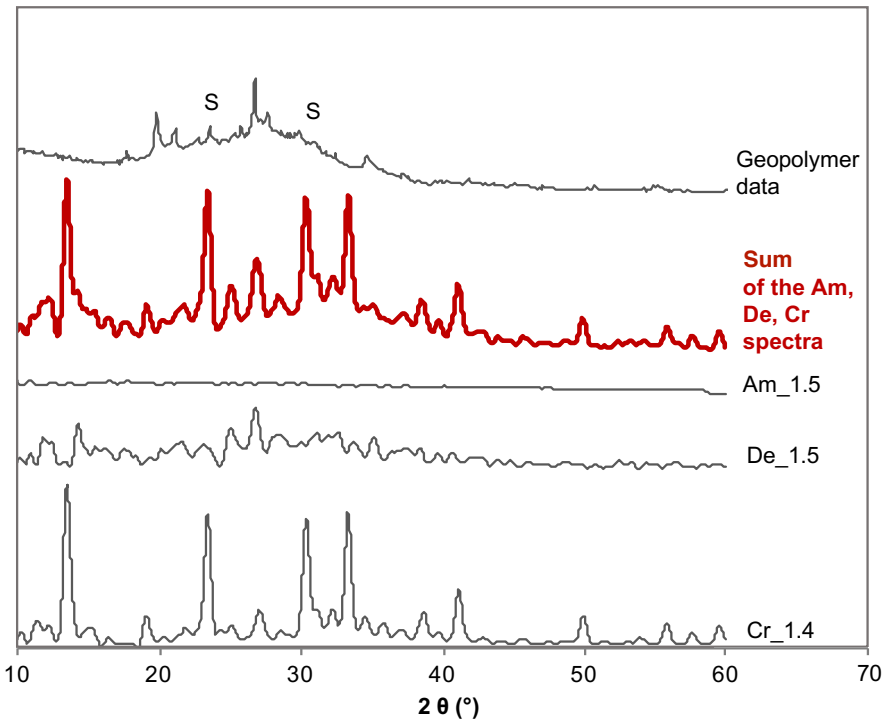

Figure 9: Simulation of X-ray diffractograms for three molecular models with Si:Al = 1.4 (crystalline structure) and Si:Al = 1.5 (amorphous and defective structures) and experimental XRD for a metakaolin geopolymer paste with Si:Al = 1.5. The metakaolin used is synthesised in the laboratories of Centro Ceramico (BO, Italy). Theoretical peaks for a siliceous sodalite structure.[57] All simulated X-ray diffraction are at room temperature and ambient pressure. Legend: S = theoretical sodalite peaks.

of the level of disorder, but it is most visible from the crystalline structure, whose results are therefore shown in Fig. 10. The shift is due to the swelling of the simulation box caused by the additional water. Since three H_2O molecules for each Na atom are considered, and since one Na atom is added for each Al atom, Cr_2 contains less water and consequently the crystalline planes are closer and the angle is shifted towards higher values.

3.3 X-ray pair distribution function (PDF)

X-ray pair distribution functions from simulations and experiments are compared in Fig. 11. The experimental data were discussed up to the first-neighbour peaks, hence the analysis of the simulations here are focused on the same peaks. All the model structures, irrespective

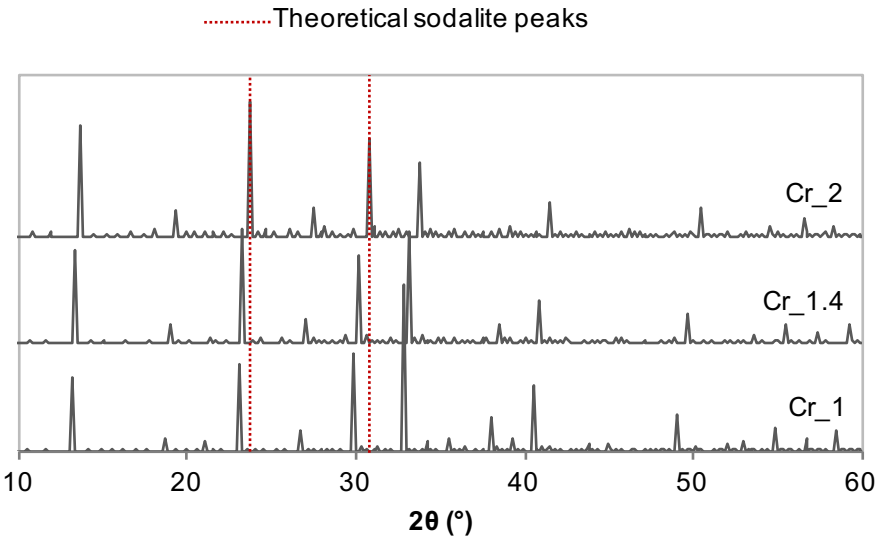

Figure 10: Simulated X-ray diffraction patterns of the three crystalline structures, varying Si:Al and showing the effect of the added water and Na. The curve for Cr_1.4 here is the same one as in Fig. 9, but here the spectrum is shown without peak broadening.

of their degree of disorder, capture two of the experimental peaks in Fig. 11.

- *T-O peak ($r \approx 1.7$ Å).* The X-ray pair distribution function obtained from simulation discerns between peaks associated with Si and Al tetrahedra, whereas the experiment displays a single broader peak. This difference may be due to two factors combined: the limited resolution of the experiment compared to the molecular model, and the possibility that the Force Field in the simulations might slightly overconstrain the interatomic distances to their equilibrium positions compared to the experiment. As expected, the level of disorder does not affect significantly these peaks in the simulations, because they depend only on the tetrahedral coordination of Al and Si with O.

- *O-O peak ($r \approx 2.7$ Å).* All the simulations display and correctly locate the first O-O peak, which depends on the relative position of neighbouring tetrahedra as well as on the location of water molecules.

Conversely, two of the experimental peaks in Fig. 11 are captured only by the defective

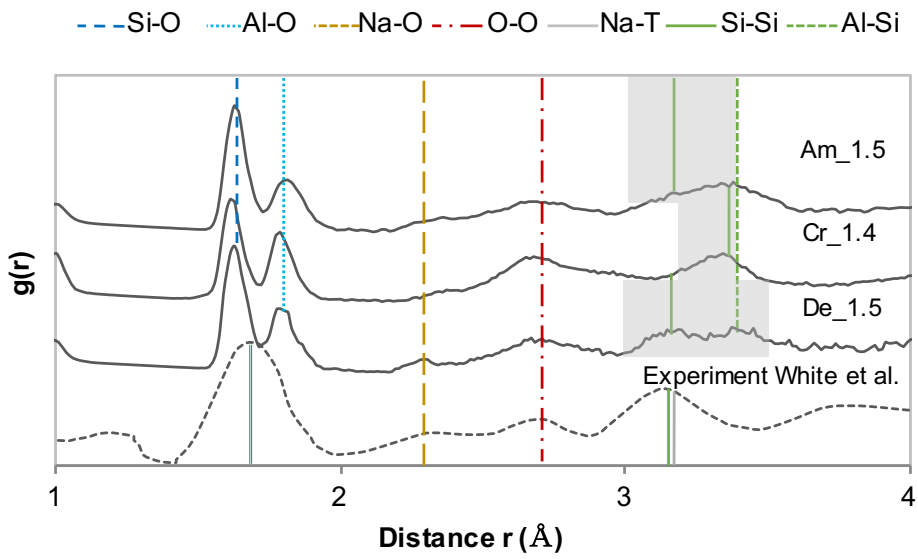

Figure 11: X-ray pair distribution function of metakaolin-based geopolymers. Comparison between experiments[13] and simulations on structures with Si:Al = 1.4 and 1.5. T: tetrahedral (Si or Al).

model structure:

- *Na-O peak ($r \approx 2.3$ Å).* The defective structure is the only one clearly capturing this peak. In sodalite-based zeolites, the cations tend to occupy the center of ring structures; it is likely that the fact that the Na-O peak emerges only in the defective structure is related to its broader distribution of ring sizes compared to the amorphous and crystalline structures (see Fig. 7).

- *Na-T and T-T peaks ($r \approx 3.2$ Å).* The experiment indicates a single broad peak encompassing all the Na-T and T-T first neighbour peaks, and centred at ≈ 3.1 Å. The crystalline structure displays a similar cumulative peak but shifted towards 3.3 Å. The amorphous structure displays a broader peak between 3 and 3.5 Å, resulting from the convolution of a broad Na-T peak, a Si-Si peak centred at 3.1 Å, and a sharp Si-Al peak at 3.3 Å. The defective structure is similar to the amorphous, to some extent, but the Al-Si peak at 3.3 Å is less sharp and broader, whereas the Si-Si peak at 3.1 Å is more marked. As a result, the overall PDF clearly shows the presence of a peak at 3.1 Å,

as in the experiment. This indicates that the positions of the peaks at *ca.* 3.2 Å are sensitive to the level of disorder, and that the intermediate disorder in the defective structure goes in the right direction of reducing the intensity of the Al-Si peak while increasing the intensity of the Si-Si peak. The agreement with the experiment leaves room for improvement, in that even in the defective structure the Si-Si and Si-Al peaks have similar intensity, whereas the experiment shows a prevalent peak at 3.1 Å (Si-Si). However, this limited difference in some T-T distances is not expected to cause any significant inaccuracy in the skeletal density and mechanical properties that will be evaluated next in this manuscript.

3.4 Wet skeletal density

Table 3: Skeletal density of metakaolin geopolymers considering structural water (Wet ρ_{sk}). The literature data were obtained by He-pycnometry tests,[58] comparing nominal density and pore volume[25] and from simulations on a fully glassy model structure.[11]

Literature data	Si:Al	Wet ρ_{sk} (g/cm^3)
Šmilauer et al., 2011[58]	1.22	2.372
Duxson et al., 2007[25]	1.15 - 1.65	1.8 - 1.7
Sadat et al, 2016[11]	1-2	2.03 - 2.50

The wet skeletal density includes the so-called structural water (see Methodology); the simulations in this work predict wet skeletal densities between ∼2.2 and ∼ 2.3 g/cm^3, which are in line with literature results (see Table 3). Fig. 12 shows the trend of density as a function of the Al:Si (and Si:Al) molar ratios. The higher the Al:Si ratio is, the more Na and thus water molecules are added to the structure (to keep the molar ratios Al:NA:H_2O to 1:1:3 as explained in Section 2.2). The values at Al:Si = 0 coincide with the densities of the siliceous baseline structures computed in Section 3.1. The density of the crystalline structure increases significantly with the Al:Si ratio, this is due to the presence of large pores, with width of *ca.* 6.5 Å (see pore size distribution in Fig. 8). These pores can accommodate Na and H_2O molecules, hence additional mass, without any significant increase of the volume

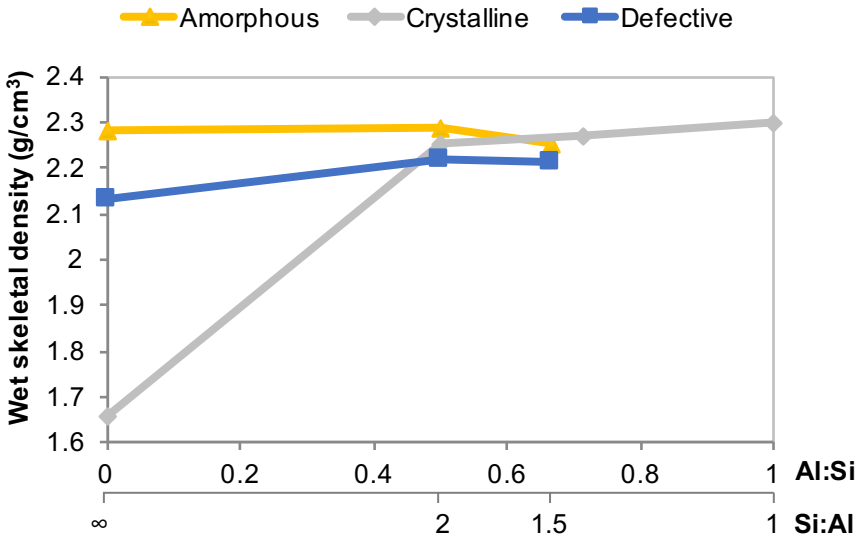

Figure 12: Wet skeletal density as function of the Al:Si and Si:Al ratio.

of the structure. On the opposite hand, the amorphous structure has only narrow pores, therefore the addition of Na and H_2O, when the Al:Si is increased, requires some swelling of the structure. This compensation effects leads to similar densities at different Al contents, and even a slight decrease as the Al:Si increases (due to the lower density of water compared to Al and Si). The defective structure sits in between the other two: a moderate addition of Al, *viz* at Al:Si < 0.5 (so Si:Al > 2) causes an increase of density similar to that of the crystalline structure, although less marked because only several "large" pores with width of *ca* 6.5 Å remain in the defective structure (see Fig. 11). Further increasing of the Al:Si ratio instead requires the defective structure to swell, hence the density stabilises and even decreases slightly for Al:Si > 0.5, similar to the trend displayed by the amorphous structure in the same range of Al:Si ratios.

3.5 Mechanical properties: elastic modulus

Fig. 13 shows the elastic moduli of all the model structures in this paper, averaged over the three Cartesian axes. The moduli of the crystalline structure are clearly the largest, followed by the defective structure and then closely by the amorphous ones. This indicates

that the level of structural disorder has an important impact on the elastic moduli at the molecular scale. The chemical composition, here quantified by the Si:Al ratio, also plays a role. Literature data from macroscale experiments indicate that E increases with Si:Al.[25] An analogous, albeit weak, trend emerges overall from the simulations, with the crystalline structure showing a clear increase going from Si:Al = 1 to 1.5, and the amorphous and defective structures showing a mild increase from Si:Al = 1.5 to 2. On the other hand, one should note that the experimental measurements are on macroscopic samples, thus the trend in E may be affected by heterogeneities at larger length scales (*e.g.* microstructural characteristics) that molecular simulations cannot describe. The wet skeletal density instead appears not to be a good predictor of trends in elastic moduli, unlike often observed in materials with similar chemical compositions at the macroscale. Indeed, by comparing Fig. 13 with Fig. 12 one can immediately appreciate that an increase in Si:Al ratio (Fig. 12 read from right of left) corresponds to a decrease, whereas Fig. 13 shows that the Young modulus increases. This means that chemistry and topology at the molecular scale play an important role in determining the elastic properties of the geopolymer binder on a corresponding length scale, providing possible targets for material optimisation working up from the nanoscale.

Table 4 summarises data on Young's modulus available in the literature. Using nanoindentation, Němeček et al.[59] measured an elastic modulus of ∼18 GPa for a N-A-S-H geopolymerisation product: these measurements, however, include mesopores with size of several nanometres, which are not described by the molecular simulations presented here. To extrapolate the experimental nanoindentation results to an equivalent elastic modulus without mesopores, one can consider the gel solid fraction of 0.6[58] indicated for the same experiment. Extrapolation to zero mesoporosity (*viz.* a solid fraction of 1) using both the self-consistent and Mori Tanaka homogenisation schemes (see Constantinides et al.[42]) are shown in Table 4. The simulation results in the present paper are indeed in line with the extrapolated nanoindentation results. Table 4 also shows that literature results from molecular simulations on zeolites, such as chlorosodalite[60] and analcime,[61] are also in the same range, as well as results

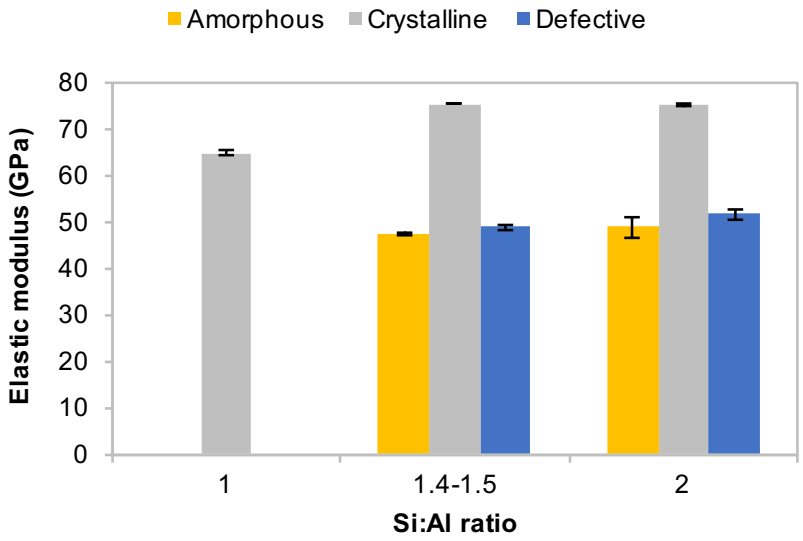

Figure 13: Young's elastic moduli as functions of the Si:Al ratio. Each elastic modulus is averaged over the three Cartesian directions.

from previous MD simulation of glassy geopolymer gels.[11]

Table 4: Literature data for the elastic modulus (GPa), from *simulations and **experiments.

	E (GPa)
**Němeček et al., 2011[59] - Mori Tanaka	44±12
**Němeček et al., 2011[59] - Self consistent	88±23
*Sadat et al., 2016[11] - glassy model structure	60 - 90
*Sanchez-Valle et al., 2005[61] - analcime	75
*Williams et al., 2006[60] - chlorosodalite	85

3.6 Mechanical properties: large-strain tensile behaviour

Fig. 14 a illustrates the complete stress-strain graph for all the structures with Si/Al=1.4-1.5. All the structures sustain stress in the order of several GPa and strain in the order of 0.1-0.5 before leaving the initial linear elastic regime. This is typical for material structures at the molecular scale,[5,29] while defects at larger scales are responsible for the experimentally observed typical values of macroscopic strength in the order of tens of MPa and corresponding strain at the elastic limit in the order of fractions of the percent. The defective and

amorphous structures display a similar mechanical behaviour, which is markedly different from that of the crystalline structure. The crystalline structure undergoes a brittle rupture and has a higher ultimate tensile stress compared to the amorphous and defective structures. These latter, instead, are more ductile, *i.e.* they sustain a high stress for a wide range of strain (from 0.1 to 0.2 - 0.25) without sudden drops of the stress itself. In particular, the defective structures can sustain larger stress and strain compared to the amorphous structure. This implies a better ability to prevent crack propagation and failure (*viz.* fracture toughness): a property that can significantly impact the durability of the material. The different mechanical response to strain can be characterised in more detail by looking at the non-affine displacements (see description in Section 2.3). Fig. 14 b shows the accumulation of non-affine displacements as a function of applied strain, only for the Si, Al, Na and O atoms in the backbone solid structure, which are the depositories of mechanical strength. The accumulation of non-affine displacements is related to the development of irreversible deformations.[45] Typically, a small level of non-affine displacement ($\overline{\delta}_{na}$) is already accumulated during the initial linear stress-strain response of the material, due to small irreversible rearrangements that have a negligible impact on the overall mechanics and elastic moduli.[45] All the model structures presented here show such an initial small increase of $\overline{\delta}_{na}$ during the linear elastic stage (strain < 0.1). Instead, as expected, $\overline{\delta}_{na}$ increases sharply when the structures leave the linear regime and enter the regime of plastic deformations eventually leading to failure. Fig. 14 b shows that the crystalline structure accumulates the least non-affine displacement (almost zero through the whole linear elastic stage), whereas the amorphous structure has the largest $\overline{\delta}_{na}$ and the defective structure is in-between. This is a convincing trend because the ability to accumulate non-affine displacements is expected to increase with the level of disorder, whereas order and symmetry add constraints to be overcome for $\overline{\delta}_{na}$ to develop. The loss of constraints hence the better mobility (in response to strain) of atoms in the backbone structure, evidenced by the increase in $\overline{\delta}_{na}$ with the level of disorder, provides a rationale for the trend of Young elastic moduli and strength in Fig. 14 a, which are both

decreasing with the level of disorder.

The results presented in Section 3.1 have shown that the only topological feature distinguishing the amorphous structure from the defective one are the ring analysis and the pore structure. This suggests that long-range correlations extending from the molecular scale to the mesoscale of several nanometres, may play an important role in determining the large-strain and failure behaviour of geopolymers. However, as for the elastic modulus results discussed earlier, structural features at even larger scale (microstructure) are also likely to significantly impact the large-strain behaviour of the material. The results in Fig. 14 therefore should be regarded as the necessary starting point for new multi-scale models of geopolymer mechanics.

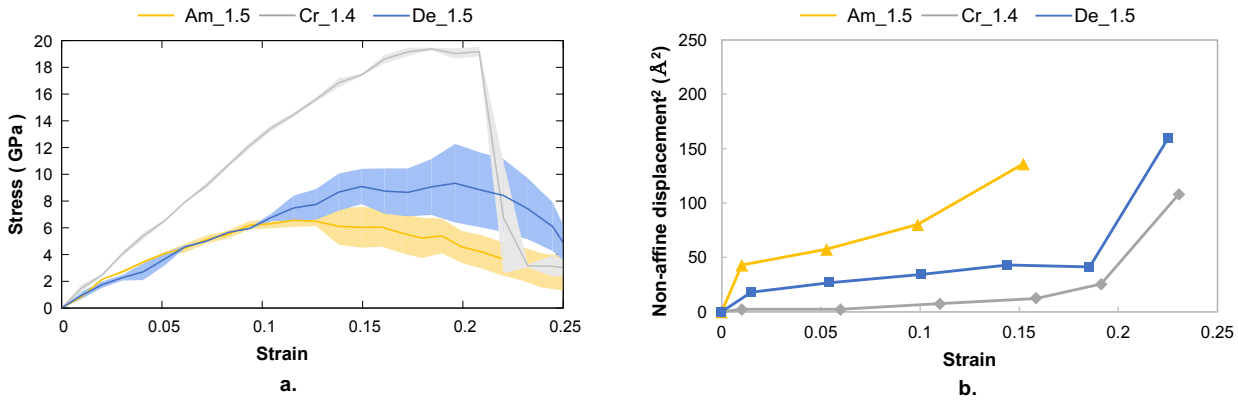

Figure 14: a. Stress-strain response under tensile load. Curves obtained from molecular dynamics simulations with strain applied in steps of 1%. Am_1.5 (amorphous with Si:Al = 1.5), Cr_1.4 (crystalline with Si:Al = 1.4) and De_1.5 (defective with Si:Al = 1.5). Each curve is obtained as the average from three repetitions; the shaded areas show the maximum and minimum stress obtained from the repetitions. b. Non-affine displacement as function of applied strain for the Si, Al, Na and O atoms in the backbone solid structure.

4 Conclusions

A new molecular model of the geopolymerisation product (N-A-S-H), obtained creating vacancies in a sodalite cage, is described in this paper. The resulting defective structures have been constructed with a range of Si:Al ratios and have been analysed in terms of structure

and mechanical properties. The same analyses have also been carried out for fully amorphous and fully crystalline model structures with analogous chemical compositions. All the structures, irrespective of their level of disorder, respected a set of crystallographic constraints including Loewenstein's principle, full Q^4 polymerisation, and absence of edge-sharing tetrahedra. The main findings are:

- The crystalline structure significantly differs from both the amorphous and defective ones in terms of bond angle, bond length, and ring size distributions and the pore structure analysis. By contrast, only the ring size distribution distinguish the amorphous from the defective structures.

- In terms of XRD spectrum, the defective structure combines an overall amorphous character, namely a broad halo peak over a wide range of $2\theta = 20°$-$30°$ angles with sharp peaks that are typical of crystalline features.

- In terms of X-ray pair distribution function, several peaks are captured by all structures irrespective of their level of disorder. However, only the defective structure captures the Na-O peak at 2.3 Å . Also, the defective structure is the one that best captures the position and impact of the Si-Si peak, at 3.1 Å , on the overall signal. This result may be a consequence of the unique character of the ring size distribution for the defective structure, where rings can be much larger compared to those in the amorphous and crystalline structures.

- The wet skeletal densities of all the model structures in this paper are in the range of experimental results from the literature. The trends of density with content in aluminum have been explained based on the pore size distribution of the baseline siliceous structures. In particular, the filling large pores (*ca.* 6.5 Å in width) with water and sodium in the crystalline structure and, to a lesser extent, in the defective structure, explain the trend of increasing density with increasing Al:Si ratio.

- In terms of the mechanics, the initial linear elastic stress-strain behaviour is characterised by Young moduli between 45 and 75 GPa, which are in the range of experimental results. The moduli are largest for the crystalline structure and lowest for the amorphous one, showing a mildly increasing trend with increasing Si:Al ratio. Density instead is shown not to be correlated with modulus: degree of order and chemical composition play a more important role. The mechanical behaviour at large strain indicates that the crystalline structure is the strongest, *i.e.* it can sustain the highest tensile load, but its failure is brittle, which is an important drawback in that it favours crack initiation and propagation. The structural disorder in the amorphous and defective structures reduces the maximum tensile stress that can be sustained, but it also leads to a more ductile behaviour which is desirable in mechanical applications. In particular, the defective structure is superior in that it combines higher strength and ductility compared to the fully amorphous one. The analysis of non-affine displacements indicates that structural disorder enables more mobility of the atoms in the T-O backbone structure, when tensile strain is applied. This provides a rational for the observed detrimental effect of disorder on Young moduli and strength.

The molecular models presented here refer to N-A-S-H obtained from a high-purity metakaolin precursor activated with typical sodium-based solutions. The approach to obtain those structure, however, is general and transferrable to modelling geopolymers from other precursors or activating solutions, *e.g.* low-calcium fly ash and potassium-based solutions. Even if complemented with additional chemical features, *e.g.* impurities, and directed towards other application-specific geometries, the approach presented here would retain its ability to link chemistry and molecular structure with mechanical performance. By linking chemical composition with structural features, density, and mechanical properties, this manuscript is a starting point for the development of larger scale models of geopolymers. Multi-scale models are the key to clarify which fundamental mechanisms control the chemo-mechanical stability and durability of these materials, and how these mechanisms are affected

by chemical composition and processing.[8,62,63] Ultimately, this will enable the simulation-guided optimisation of geopolymer cements, the generation of confidence in their long-term performance, and the development of adequate design standards to support the deployment of these more sustainable cements in the construction sector.

Acknowledgement

The contributions of John L. Provis were funded by the European Research Council under the European Union's Seventh Framework Programme (FP7/2007-2013)/ERC Grant Agreement #335928 (GeopolyConc).

Hegoi Manzano acknowledges the financial support from the Departamento de Educación, Política Lingüística y Cultura del Gobierno Vasco (IT912-16) and the ELKARTEK project.

References

(1) Davidovits, J. Geopolymers. *J. Therm. Anal.* **1991**, *37*, 1633–1656.

(2) Habert, G.; Ouellet-Plamondon, C. Recent Update on the Environmental Impact of Geopolymers. *RILEM Technical Letters* **2016**, *1*, 17–23.

(3) Pacheco-Torgal, F.; Abdollahnejad, Z.; Camões, A. F.; Jamshidi, M.; Ding, Y. Durability of Alkali-Activated Binders: A Clear Advantage over Portland Cement or an Unproven Issue? *Constr. Build. Mater.* **2012**, *30*, 400–405.

(4) Provis, J. L.; Duxson, P.; Van Deventer, J. S. J.; Lukey, G. C. The Role of Mathematical Modelling and Gel Chemistry in Advancing Geopolymer Technology. *Chem. Eng. Res. Des.* **2005**, *83*, 853–860.

(5) Manzano, H.; Moeini, S.; Marinelli, F.; van Duin, A. C. T.; Ulm, F.-J.; Pellenq, R. J. M. Confined Water Dissociation in Microporous Defective Silicates: Mechanism,

Dipole Distribution, and Impact on Substrate Properties. *J. Am. Chem. Soc.* **2012**, *134*, 2208–2215.

(6) Papatzani, S.; Paine, K.; Calabria-Holley, J. A Comprehensive Review of the Models on the Nanostructure of Calcium Silicate Hydrates. *Constr. Build. Mater.* **2015**, *74*, 219–234.

(7) Hajilar, S.; Shafei, B. Nano-Scale Investigation of Elastic Properties of Hydrated Cement Paste Constituents using Molecular Dynamics Simulations. *Comput. Mater. Sci.* **2015**, *101*, 216–226.

(8) Pinson, M. B.; Masoero, E.; Bonnaud, P. A.; Manzano, H.; Ji, Q.; Yip, S.; Thomas, J. J.; Bazant, M. Z.; Van Vliet, K. J.; Jennings, H. M. Hysteresis from Multiscale Porosity: Modeling Water Sorption and Shrinkage in Cement Paste. *Phys. Rev. Appl.* **2015**, *3*, 064009.

(9) Ioannidou, K.; Krakowiak, K. J.; Bauchy, M.; Hoover, C. G.; Masoero, E.; Yip, S.; Ulm, F.-J.; Levitz, P.; Pellenq, R. J.-M.; Del Gado, E. Mesoscale Texture of Cement Hydrates. *Proc. Natl. Acad. Sci.* **2016**, *113*, 2029–2034.

(10) Bauchy, M.; Wang, M.; Yu, Y.; Wang, B.; Krishnan, N. M. A.; Masoero, E.; Ulm, F.-J.; Pellenq, R. Topological Control on the Structural Relaxation of Atomic Networks under Stress. *Phys. Rev. Lett.* **2017**, *119*, 035502.

(11) Sadat, M. R.; Bringuier, S.; Asaduzzaman, A.; Muralidharan, K.; Zhang, L. A Molecular Dynamics Study of the Role of Molecular Water on the Structure and Mechanics of Amorphous Geopolymer Binders. *J. Chem. Phys.* **2016**, *145*, 134706.

(12) White, C. E.; Provis, J. L.; Proffen, T.; van Deventer, J. S. J. Molecular Mechanisms Responsible for the Structural Changes Occurring during Geopolymerization: Multiscale Simulation. *AIChE Journal* **2012**, *58*, 2241–2253.

(13) White, C. E.; Page, K.; Henson, N. J.; Provis, J. L. In Situ Synchrotron X-ray Pair Distribution Function Analysis of the Early Stages of Gel Formation in Metakaolin-Based Geopolymers. *Appl. Clay Sci.* **2013**, *73*, 17–25.

(14) Fernàndez-Jimènez, A.; Monzó, M.; Vicent, M.; Barba, A.; Palomo, A. Alkaline Activation of Metakaolin and Fly Ash Mixtures: Obtain of Zeoceramics and Zeocements. *Microporous Mesoporous Mater.* **2008**, *108*, 41–49.

(15) Kriven, W. M.; Gordon, M.; Bell, J. L. Geopolymers: Nanoparticulate, Nanoporous Ceramics Made Under Ambient Conditions. *Microsc. Microanal.* **2004**, *10*, 404–405.

(16) Provis, J. L.; Lukey, G. C.; van Deventer, J. S. J. Do Geopolymers Actually Contain Nanocrystalline Zeolites? A Reexamination of Existing Results. *Chem. Mater.* **2005**, *17*, 3075–3085.

(17) Duxson, P.; Provis, J. L.; Lukey, G. C.; Separovic, F.; van Deventer, J. S. J. 29Si NMR Study of Structural Ordering in Aluminosilicate Geopolymer Gels. *Langmuir* **2005**, *21*, 3028–3036.

(18) Favier, A.; Habert, G.; Roussel, N.; d'Espinose de Lacaillerie, J.-B. A Multinuclear Static NMR Study of Geopolymerisation. *Cem. Concr. Res.* **2015**, *75*, 104 – 109.

(19) Plimpton, S. Fast Parallel Algorithms for Short-Range Molecular Dynamics. *J. Comput. Phys.* **1995**, *117*, 1–19.

(20) Le Roux, S.; Petkov, V. ISAACS - Interactive Structure Analysis of Amorphous and Crystalline Systems. *J. Appl. Crystallogr.* **2010**, *43*, 181–185.

(21) Pinheiro, M.; Martin, R. L.; Rycroft, C. H.; Jones, A.; Iglesia, E.; Haranczyk, M. Characterization and Comparison of Pore Landscapes in Crystalline Porous Materials. *J. Mol. Graph. Model* **2013**, *44*, 208–219.

(22) Willems, T. F.; Rycroft, C. H.; Kazi, M.; Meza, J. C.; Haranczyk, M. Algorithms and Tools for High-Throughput Geometry-Based Analysis of Crystalline Porous Materials. *Microporous Mesoporous Mater.* **2012**, *149*, 134–141.

(23) Martinez, L.; Andrade, R.; Birgin, E.; Martinez, J. PACKMOL: A Package for Building Initial Configurations for Molecular Dynamics Simulations. *J. Comput. Chem.* **2009**, *30*, 2157–2164.

(24) Momma, K.; Izumi, F. VESTA 3 for Three-Dimensional Visualization of Crystal, Volumetric and Morphology Data. *J. Appl. Crystallogr.* **2011**, *44*, 1272–1276.

(25) Duxson, P.; Lukey, G. C.; van Deventer, J. S. J. Physical Evolution of Na Geopolymer Derived from Metakaolin up to 1000 C. *J. Mat. Sci.* **2007**, *42*, 3044–3054.

(26) Kuenzel, C.; Vandeperre, L. J.; Donatello, S.; Boccaccini, A. R.; Cheeseman, C. Ambient Temperature Drying Shrinkage and Cracking in Metakaolin-Based Geopolymers. *J. Am. Ceram. Soc.* **2012**, *95*, 3270–3277.

(27) Duxson, P. The Structure and Thermal Evolution of Metakaolin Geopolymers. Ph.D. thesis, Department of Chemical and Biomolecular Engineering, The University of Melbourne, 2006.

(28) Senftle, T. P.; Hong, S.; Islam, M. M.; Kylasa, S. B.; Zheng, Y.; Shin, Y. K.; Junkermeier, C.; Engel-Herbert, R.; Janik, M. J.; Aktulga, H. M.; Verstraelen, T.; Grama, A.; van Duin, A. C. T. The ReaxFF Reactive Force-Field: Development, Applications and Future Directions. *Npj Comput. Mater.* **2016**, *2*, 15011.

(29) Manzano, H.; Masoero, E.; Lopez-Arbeloa, I.; Jennings, H. M. Shear Deformations in Calcium Silicate Hydrates. *Soft Matter* **2013**, *9*, 7333–7341.

(30) Manzano, H.; Masoero, E.; Lopez-Arbeloa, I.; M. Jennings, H. *Mechanics and Physics of Creep, Shrinkage, and Durability of Concrete: A Tribute to Zdeňk P. Bažant - Proceed-*

ings of the 9th Int. Conf. on Creep, Shrinkage, and Durability Mechanics, CONCREEP; 2013; pp 86–97.

(31) Fogarty, J.; Aktulga, H. M.; Grama, A.; van Duin, A.; Pandit, S. A. A Reactive Molecular Dynamics Simulation of the Silica-Water Interface. *J. Chem. Phys.* **2010**, *132*, 174704.

(32) Joshi, K.; van Duin, A. Molecular Dynamics Study on the Influence of Additives on the High- Temperature Structural and Acidic Properties of ZSM - 5 Zeolite. *Energy Fuels* **2013**, *27*, 4481–4488.

(33) Joshi, K. L.; Psofogiannakis, G.; Van Duin, A. C.; Raman, S. Reactive Molecular Simulations of Protonation of Water Clusters and Depletion of Acidity in H-ZSM-5 Zeolite. *Phys. Chem. Chem. Phys.* **2014**, *16*, 18433–18441.

(34) Bai, C.; Liu, L.; Sun, H. Molecular Dynamics Simulations of Methanol to Olefin Reactions in HZSM-5 Zeolite Using a ReaxFF Force Field. *J. Phys. Chem. C* **2012**, *116*, 7029–7039.

(35) Yu, Y.; Wang, B.; Wang, M.; Sant, G.; Bauchy, M. Reactive Molecular Dynamics Simulations of Sodium Silicate Glasses - Toward an Improved Understanding of the Structure. *Int. J. Appl. Glass Sci.* **2016**, *8*, 276–284.

(36) Sheikholeslam, S. A.; Manzano, H.; Grecu, C.; Ivanov, A. Reduced Hydrogen Diffusion in Strained Amorphous SiO2: Understanding Ageing in MOSFET Devices. *J. Mat. Chem. C* **2016**, *4*, 8104–8110.

(37) Porcher, F.; Souhassou, M.; Dusausoy, Y.; Lecomte, C. The Crystal Structure of a Low-Silica Dehydrated NaX Zeolite. *Eur. J. Mineral.* **1999**, 333–344.

(38) Manzano, H.; Dolado, J.; Ayuela, A. Elastic Properties of the Main Species Present in Portland Cement Pastes. *Acta Mater.* **2009**, *57*, 1666–1674.

(39) Baimpos, T.; Giannakopoulos, I. G.; Nikolakis, V.; Kouzoudis, D. Effect of Gas Adsorption on the Elastic Properties of Faujasite Films Measured using Magnetoelastic Sensors. *Chem. Mater.* **2008**, *20*, 1470–1475.

(40) Bryukhanov, I. A.; Rybakov, A. A.; Larin, A. V.; Trubnikov, D. N.; Vercauteren, D. P. The Role of Water in the Elastic Properties of Aluminosilicate Zeolites: DFT Investigation. *J. Mol. Model.* **2017**, *23*, 68.

(41) Palmer, D. C. *CrystalDiffract User's Guide*; CrystalMaker Software Ltd, 2015.

(42) Constantinides, G.; Ulm, F.-J. The Nanogranular Nature of C-S-H. *J. Mech. Phys. Solids* **2007**, *55*, 64 – 90.

(43) Galin, L. A.; Moss, H.; Sneddon, I. N. *Contact Problems in the Theory of Elasticity*; 1961.

(44) Timoshenko, S. *Theory of Elasticity*, 3rd ed.; Engineering societies monographs; McGraw-Hill: New York, 1969.

(45) Masoero, E.; Del Gado, E.; Pellenq, R. J.-M.; Yip, S.; Ulm, F.-J. Nano-Scale Mechanics of Colloidal C–S–H Gels. *Soft matter* **2014**, *10*, 491–499.

(46) Database of Zeolite Structures. `http://www.iza-structure.org/databases/`, Accessed: 2018-04-20.

(47) Duxson, P.; Lukey, G. C.; van Deventer, J. S. J. Evolution of Gel Structure during Thermal Processing of Na-Geopolymer Gels. *Langmuir* **2006**, *22*, 8750–8757.

(48) Slavík, R.; Bednařík, V.; Vondruška, M.; Skoba, O.; Hanzlíček, T. Proof of Sodalite Structures in Geopolymers. 3rd Meeting on Chemistry and Life. 2005.

(49) Oh, J. E.; Moon, J.; Mancio, M.; Clark, S. M.; Monteiro, P. J. Bulk Modulus of Basic Sodalite, Na8 [AlSiO4] 6 (OH) 2· 2H2O, a possible Zeolitic Precursor in Coal-Fly-Ash-Based Geopolymers. *Cem. Concr. Res.* **2011**, *41*, 107–112.

(50) Walling, S. A.; Bernal, S. A.; Gardner, L. J.; Kinoshita, H.; Provis, J. L. Phase Formation and Evolution in Mg (OH) 2–Zeolite Cements. *Ind. Eng. Chem. Res.* **2018**, *57*, 2105–2113.

(51) Sturm, P.; Gluth, G.; Simon, S.; Brouwers, H.; Kühne, H.-C. The Effect of Heat Treatment on the Mechanical and Structural Properties of One-Part Geopolymer-Zeolite Composites. *Thermochim. Acta* **2016**, *635*, 41–58.

(52) Alzeer, M.; MacKenzie, K. J. Synthesis and Mechanical Properties of New Fibre-Reinforced Composites of Inorganic Polymers with Natural Wool Fibres. *J. Mater. Sci.* **2012**, *47*, 6958–6965.

(53) Louisnathan, S. J.; Hill, R. J.; Gibbs, G. V. Tetrahedral Bond Length Variations in Sulfates. *Phys. Chem. Miner.* **1977**, *1*, 53–69.

(54) Yuan, X.; Cormack, A. N. Si-O-Si Bond Angle and Torsion Angle Distribution in Vitreous Silica and Sodium Silicate Glasses. *J. Non-Cryst. Solids* **2003**, *319*, 31–43.

(55) Baerlocher, C.; Meier, W. M.; Olson, D. *Atlas of Zeolite Framework Types*, 5th ed.; Elsevier: Amsterdam; New York, 2001.

(56) Stukowski, A. Visualization and Analysis of Atomistic Simulation Data with OVITO–the Open Visualization Tool. *Modelling Simul. Mater. Sci. Eng.* **2009**, *18*, 015012.

(57) *Collection of Simulated XRD Powder Patterns for Zeolites*, 5th ed.; Elsevier: Oxford, 2007.

(58) Šmilauer, V.; Hlavàček, P.; Škvàra, F.; Šulc, R.; Kopeckỳ, L.; Němeček, J. Micromechanical Multiscale Model for Alkali Activation of Fly Ash and Metakaolin. *J. Mat. Sci.* **2011**, *46*, 6545–6555.

(59) Němeček, J.; Šmilauer, V.; Kopeckỳ, L. Nanoindentation Characteristics of Alkali-Activated Aluminosilicate Materials. *Cem. Concr. Compos.* **2011**, *33*, 163–170.

(60) Williams, J. J.; Evans, K. E.; Walton, R. I. On the Elastic Constants of the Zeolite Chlorosodalite. *Appl. Phys. Lett.* **2006**, *88*, 021914.

(61) Sanchez-Valle, C.; Sinogeikin, S. V.; Lethbridge, Z. A. D.; Walton, R. I.; Smith, C. W.; Evans, K. E.; Bass, J. D. Brillouin Scattering Study on the Single- Crystal Elastic Properties of Natrolite and Analcime Zeolites. *J. Appl. Phys.* **2005**, *98*, 053508.

(62) Shvab, I.; Brochard, L.; Manzano, H.; Masoero, E. Precipitation Mechanisms of Mesoporous Nanoparticle Aggregates: Off-Lattice, Coarse-Grained, Kinetic Simulations. *Cryst. Growth Des.* **2017**, *17*, 1316–1327.

(63) Masoero, E.; Cusatis, G.; Di Luzio, G. C–S–H gel densification: The impact of the nanoscale on self-desiccation and sorption isotherms. *Cem. Concr. Res.* **2018**, *109*, 103–119.

Graphical TOC Entry